Ray Tracing for Jupiter's Icy Moon Ionospheric Occultation of Jovian Auroral Radio Sources

Rikuto Yasuda, Tomoki Kimura, Hiroaki Misawa, Fuminori Tsuchiya, Baptiste Cecconi, Yasumasa Kasaba, Shinnosuke Satoh, Shotaro Sakai, Corentin K. Louis

JGR Space Physics

RESEARCH ARTICLE
10.1029/2024JA032454

Ray Tracing for Jupiter's Icy Moon Ionospheric Occultation of Jovian Auroral Radio Sources

Rikuto Yasuda[1,2], Tomoki Kimura[3], Hiroaki Misawa[1], Fuminori Tsuchiya[1], Baptiste Cecconi[2], Yasumasa Kasaba[1], Shinnosuke Satoh[1], Shotaro Sakai[1,4], and Corentin K. Louis[2,5]

[1]Planetary Plasma and Atmospheric Research Center, Graduate School of Science, Tohoku University, Sendai, Japan, [2]LESIA, Observatoire de Paris, Université PSL, Sorbonne Université, Université Paris Cité, CNRS, Meudon, France, [3]Department of Physics, Faculty of Science, Tokyo University of Science, Tokyo, Japan, [4]Department of Geophysics, Graduate School of Science, Tohoku University, Sendai, Japan, [5]School of Cosmic Physics, DIAS Dunsink Observatory, Dublin Institute for Advanced Studies, Dublin, Ireland

Abstract The ionospheres of Jupiter's icy moons have been observed by in situ plasma measurements and radio science. However, their spatial structures have not yet been fully characterized. To address this, we developed a new ray tracing method for modeling the radio occultation of the ionospheres using Jovian auroral radio sources. Applying our method to Jovian auroral radio observations with the Galileo spacecraft, we derived the electron density of the ionosphere of Ganymede and Callisto. For Ganymede's ionosphere, we found that the maximum electron density on the surface was 76.5–288.5 cm^{-3} in the open magnetic field line regions and 5.0–20.5 cm^{-3} in the closed magnetic field line region during the Galileo Ganymede 01 flyby. The difference in the electron density distribution was correlated with the accessibility of Jovian magnetospheric plasma to the atmosphere and surface of the moons. These results indicated that electron-impact ionization of the Ganymede exosphere and sputtering of the surface water ice were effective for the producing Ganymede's ionosphere. For Callisto's ionosphere, we found that the densities were approximately 350 and 12.5 cm^{-3} on the night side hemisphere during Callisto 09 and 30 flybys, respectively. These results combined with previous observations indicated that atmospheric production through sublimation controlled the ionospheric density of Callisto. This method is also applicable to upcoming Jovian radio observation data from the Jupiter Icy Moon Explorer, JUICE.

Key Points:

- We developed a ray tracing method for Jupiter's icy moon ionospheric occultation of Jovian auroral radio sources
- The ionospheric density of Ganymede is associated with electron-impact ionization and atmospheric production via ion sputtering
- The Ionospheric density of Callisto is associated with atmospheric production by solar illumination on its surface

Correspondence to:
R. Yasuda,
yasuda.r@pparc.gp.tohoku.ac.jp

Citation:
Yasuda, R., Kimura, T., Misawa, H., Tsuchiya, F., Cecconi, B., Kasaba, Y., et al. (2024). Ray tracing for Jupiter's icy moon ionospheric occultation of Jovian auroral radio sources. *Journal of Geophysical Research: Space Physics*, *129*, e2024JA032454. https://doi.org/10.1029/2024JA032454

Received 15 JAN 2024
Accepted 7 MAY 2024

1. Introduction

The ionospheres of Jupiter's icy moons (Europa, Ganymede, and Callisto) have been characterized by numerical modeling and spacecraft observation. Each ionosphere has a unique structure associated with its formation process, and it is generated by the production of a neutral atmosphere (atmospheric supply) and the ionization of the neutral atmosphere. The neutral atmosphere is produced by surface material sputtering with charged particles in the Jovian magnetosphere (Leblanc et al., 2017; Shematovich & Johnson, 2001; Vorburger et al., 2015) and sublimation by solar irradiation (Shematovich et al., 2005; Vorburger et al., 2015, 2022). Liquid water spouted from the interior can also contribute to atmospheric production (Arnold et al., 2020; Huybrighs et al., 2020; Jia et al., 2018; Li et al., 2020). The neutral atmosphere is ionized by the following two processes: electron-impact ionization with energies above tens of eV and photoionization with solar extreme ultraviolet (EUV) radiation (Carnielli et al., 2019). These ionospheric formation processes control the ionospheric structure of the icy moons.

Galileo and Juno observations attempted to characterize the structure and formation process of the ionosphere. The ionospheric density structures of Ganymede, Callisto, and Europa were estimated by "Radio science," which is a method of measuring the total electron content along a path from the spacecraft to the Earth using the frequency shift of telecommunication radio waves. Galileo radio science observations confirmed dense ionospheres under a sunlit trailing hemisphere, where Jupiter's magnetic field and plasma collided with the moon (Kliore et al., 2002; McGrath et al., 2004). These authors suggested that the atmosphere was potentially created by sputtering and then ionized by solar EUV photons. The Juno spacecraft also provided electron density profiles of Ganymede's ionosphere using the radio science (Buccino et al., 2022). They found that the electron-impact ionization plays a significant role in formation of the Ganymede ionosphere because Juno detected the ionosphere only in regions where the magnetic field lines are open, allowing magnetospheric electrons to collide with the atmosphere. Galileo in situ plasma observations have also provided constraints on the structure and sources of

the ionospheres. Gurnett, Kurth, Roux, et al. (1997); Gurnett et al. (2000) derived the electron density of Callisto's ionosphere. They found increases in electron density on the day side ionosphere and no increases were observed on the night side ionosphere. They speculated that the solar irradiation was an important controlling factor of the electron density. In Ganymede's ionosphere, only two flybys of the moon provided a signature of ionospheric plasma (Eviatar, Strobel, et al., 2001; Eviatar, Vasyliunas, & Gurnett, 2001; Gurnett et al., 1996). In situ observations were also made at Europa by Kurth et al. (2001), but they did not detect any significant ionospheric signals. Although the ionospheric density was partially constrained by the above-described previous studies, the horizontal and vertical density distributions are still unclear, and the suggested ionospheric formation processes are, therefore, still debatable.

These previous observation methods have several limitations in constraining global density distributions. Radio science observations can be performed only near the day-night terminator since the Earth is in approximately the same direction as the sun, as seen from the spacecraft at the icy moons. This causes an observational restriction with respect to the solar phase angle during ionospheric observations, causing difficulty to evaluate the effects of sublimation on the atmosphere and photoionization on the ionosphere. In situ plasma observations are also spatially limited because they are performed only at the altitude where the spacecraft is located. Thus, a new method needs to be developed to compensate for these disadvantages.

Around these icy moons, radio waves emitted from Jupiter's polar regions have been observed. The Jovian radio waves ranging from a few hundred kHz to a few MHz are refracted by the ionosphere of icy moons or occulted by the moon body. We propose a new method to estimate the ionospheric density by observations of those radio waves with spacecraft. In this paper, we refer to occultations of Jupiter's radio waves by icy moons and our measurement method with the occultation as "Jovian radio occultation." Though some papers refer to "radio science" using the telecommunication radio waves in the GHz band as "radio occultation" we refer to the previous method as "Radio science" It should be noted that "radio science" and "Jupiter radio occultation" are entirely different methods since they use different radio sources, frequencies, and measurement techniques.

We developed a new ray tracing simulation for modeling Jovian radio occultation of the ionospheres of Jupiter's icy moons. This simulation enabled the use of Jovian radio occultation. Applying this method to observations performed by Galileo Plasma Wave Subsystem (GLL/PWS), we derived the electron density of the ionosphere of Ganymede and Callisto. In this study, the simulation and the methods are described in Section 2. In Section 3, we present a detail example the observation results obtained with our method. We present all results obtained by adapting the method to the Galileo spacecraft data for the icy moon flybys in Section 4. Based on the observation results, conditions for the ionospheric formation are discussed in Section 5. In Section 6, we summarize the results from this study and discuss future perspectives.

2. Jovian Radio Occultation

When the spacecraft passes the anti-Jovian side of the moon, it observes Jovian radio occultations by the icy moons (Cecconi et al., 2021; Kurth et al., 1997). Figure 1 shows a schematic view of Jovian radio occultation. Jovian radio waves are refracted in the ionosphere, and a higher electron density in the ionosphere correlates to more largely refracted radio waves (blue lines in Figure 1). This results in a wide range of undetectable positions where the observer cannot detect Jovian radio waves (red dashed lines in Figure 1). From the time of the Jovian radio occultation, we can estimate the ionospheric electron density.

In our Jovian radio occultation, spacecraft can observe the ionosphere over a wide range of solar phase angles, which reduces the observational restriction from previous radio science observations at solar phase angles. Our occultation method can measure the electron density at lower altitudes; this included altitudes lower than the lowest altitude of the spacecraft during flybys. The densities at lower altitudes cannot be measured using the in situ observations. Therefore, our method can be used to estimate the global density distributions of the ionospheres in the icy moons.

To establish Jovian radio occultation measurements, we develop a numerical model for the ionospheric occultation of Jupiter's auroral radio emissions. This model reproduces the occultation time depending on the ionospheric density distribution. We estimated the density based on a comparison of the modeled occultation time with the observation of Jovian auroral radio emissions during the flybys at the icy moons. We describe the details of the numerical model and the ionospheric density estimation method.

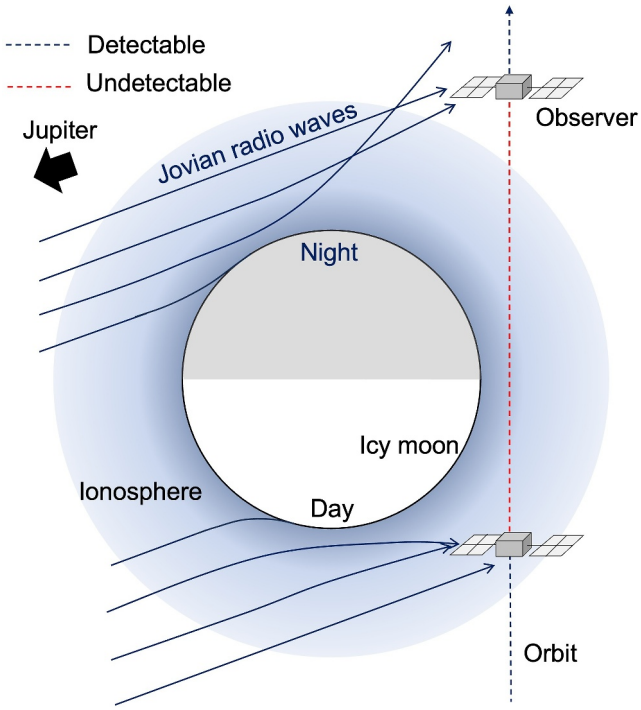

Figure 1. Schematic figure of radio occultation observation method using Jupiter's radio waves. Jovian radio waves (the blue solid line) are refracted in the ionosphere of the moons. The observer can detect the radio waves only when it is in the detectable position (the blue dashed line) and cannot detect the wave when it's in the undetectable position (the red dashed line). The detectable position is varied with the electron density profiles on the radio path between Jupiter and the spacecraft.

2.1. Radio Source Modeling

Jovian radio waves ranging from a few kHz to approximately 40 MHz are generated through the Cyclotron Maser Instability (CMI) (Louarn et al., 2017, 2018; Zarka, 2004). The CMI is a plasma instability that generates coherent radio emissions when the electron's velocity distribution function has an unstable non-Maxwellian form. The emitted radio waves have strong anisotropy in the beaming pattern, limiting the source positions of the visible radio waves (Cecconi et al., 2021; Louis et al., 2019).

The ExPRES code (Exoplanetary and Planetary Radio Emission Simulator, Louis et al., 2019) provides the positions of the visible radio sources. In the frame of CMI theory, radio emissions radiate toward a certain angle relative to the local magnetic field. The angle is determined from the electron's unstable velocity distribution function. Thus, the visible source position can be estimated by assuming a magnetic field and an electron velocity distribution. The beaming pattern and geometrical visibility conditions are illustrated in Figures 1 and 2 of Louis et al. (2019). Cecconi et al. (2021) modeled the radio emission occultations during Galileo's flyby at the Galilean moons using the ExPRES model. They showed that the ExPRES code accurately modeled the visibility of sources and the temporal occurrence of occultations observed by GLL/PWS. These authors suggested that discrepancies between the predicted and observed occultation times were attributed to refraction effects, which were not included in the ExPRES modeling scheme.

We used the visible source positions in Cecconi et al. (2021) and further considered refraction of radio waves from each source position with a ray tracing model; this progress was described in Section 2.2. The target radio frequencies in Cecconi et al. (2021) were in 42 channels, ranging from 0.1 to 5.7 MHz. The radio waves emitted above Jupiter's main auroral oval were modeled with the configurations listed in Table 1. Io-induced radio emissions were also modeled with the configurations listed in Table 1.

When a spacecraft is near the magnetic equator, the visible radio sources are classified into four types, called A, B, C, and D, corresponding to the north-eastern, north-western, south-eastern, and south-western sources, respectively, in Jupiter's polar region as observed from the spacecraft (see, Figure 2 of Marques et al. (2017), for a definition). We modeled the occultations for each of the four types of radio sources.

The source positions in Cecconi et al. (2021) were modeled every minute. To improve the precision of the modeled occultation time, we linearly interpolated the source positions from the same source type at the same frequency between the time steps and simulated radio occultation with a temporal resolution of 1 s.

2.2. Ray Tracing

To model the ionospheric occultation of radio emissions, we need to calculate the propagation paths of the radio waves around the icy moons from the sources predicted by ExPRES. In cold magnetized plasma, the radio paths depend on the plasma density and magnetic field vector. To simulate the paths, we adopt a ray tracing method

Table 1
Configuration of ExPRES Code for Jovian Radio Emission (Cecconi et al., 2021)

Magnetic field model	JRM09 magnetic field model (Connerney et al., 2018)
Examined source positions	Every 1° in longitude Magnetic field lines of M shell = 30
Unstable electron temperature	5 keV
Electron velocity distribution type	Loss cone
Source of positional data for observers and Jupiter	NASA-JPL instance of WebGeoCalc (Acton et al., 2018)

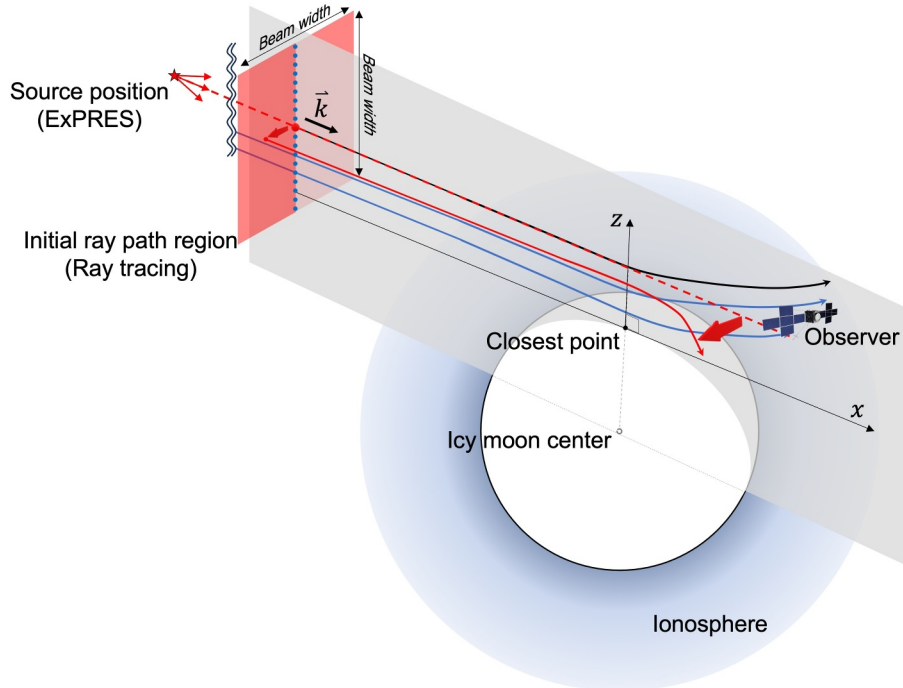

Figure 2. 3D positional relationship of a radio source, an observer, and the icy moon. The propagation path of straight radio waves from the point source position (the red dot) predicted in the ExPRES model and the actual refracted repropagation path (Black solid line). To examine detectable radio waves for the observer, we traced the radio waves emitted from the wide initial ray path region (the red shade). Radio waves propagating on the plane connecting the observer, the icy moon center, and the point source position are detectable (blue solid line) and waves propagating on the other positions cannot be observed (red solid lines).

(Kimura et al., 2008a, 2008b, 2011). This method can calculate ray paths that satisfy the dispersion relation of plasma waves in magnetized cold plasma (i.e., the Appleton–Hartree formula). In the following paragraphs, we describe the input parameters required for ray tracing (electron density, magnetic field vector, frequency of the radio waves, initial position, and initial wavenumber vector).

We assumed that the ionospheric electron density follows a spherically symmetric diffusion equilibrium distribution:

$$n_e(z) = n_{max} \exp\left(-\frac{z}{h_{scale}}\right) (\mathrm{cm}^{-3}) \quad (1)$$

where n_e is the electron density at an altitude of z, n_{max} is the maximum electron density on the surface, and h_{scale} is the scale height of the ionosphere. We model the ray paths in various ionospheric model cases by changing the maximum electron density n_{max} and the scale height h_{scale}. We assumed that the magnetic field magnitude is approximately zero in the simulation box because the local cyclotron frequency is much lower than the radio frequency. The radio frequencies are the same as those of the ExPRES outputs described in Section 2.1. The ExPRES model assumes that the propagation path is a straight line that connects the radio source position with a given observer (the red dashed line in Figure 2). If the beaming pattern of the radio emission is extremely thin, the radio waves are refracted and not detected at the observer position (the black solid line in Figure 2). The beaming pattern of typical CMI radio emission is actually a hollow conical beam with a thickness of a few degrees, and a part of the waves propagate close to the surface of the icy moon. The radio waves near the surface are refracted in the ionosphere and detected at the observer position (the blue lines in Figure 2). To model the wide beam, we trace multiple radio waves at 2 km intervals from the wide initial ray path region in the simulation box (the red shade in Figure 2). The spatial intervals are set to be smaller than the travel distance of the Galileo spacecraft in the time step of our occultation model to ensure accuracy in the modeled time. The ExPRES model (Cecconi et al., 2021; Hess et al., 2008) assumes that the thickness of the emission cone is 1° at the source region, which corresponds to

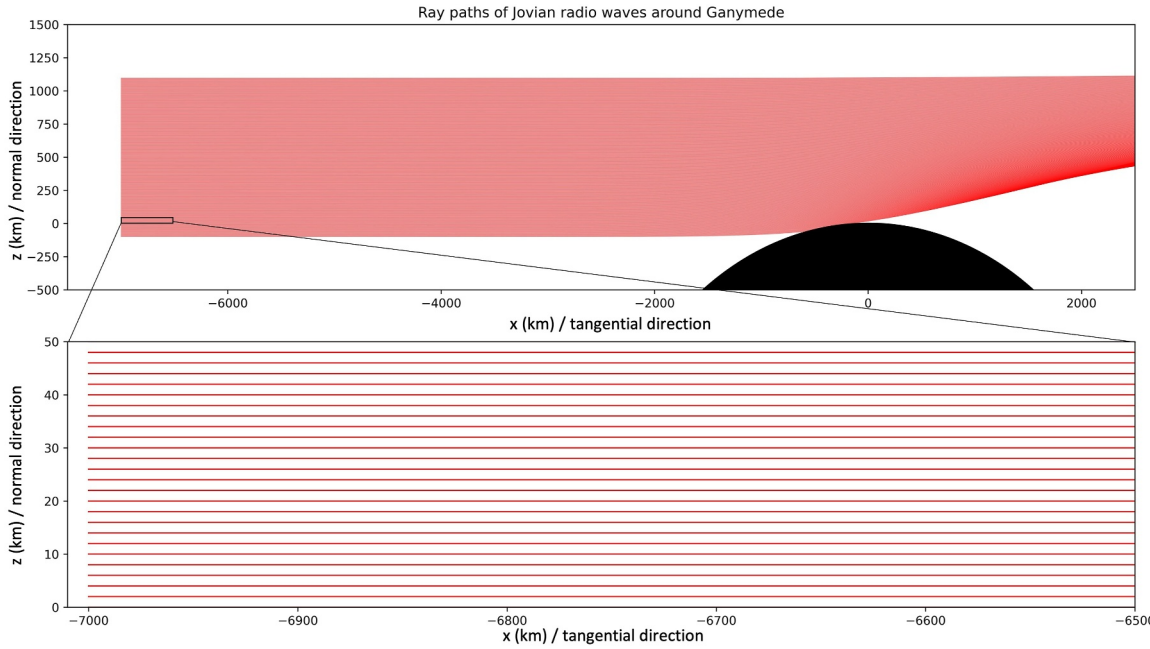

Figure 3. Ray paths around Ganymede calculated with the ray tracing method. We trace the parallel paths at 2 km intervals from far away in the negative x region. The frequency of the radio waves is 5.350 MHz. The maximum density of Ganymede ionosphere is 200 cm^{-3} and the scale height is 300 km.

beam widths of 11,713, 18,682, and 32,859 km at Europa, Ganymede, and Callisto, respectively (product of the thickness with a semimajor axis of the moon). We therefore assumed that the size of the initial ray path region was the same as the beam width at the moons (e.g., 11,713 × 11,713 km at Europa). The initial wave vectors were the same as those estimated by ExPRES, which was the direction from the estimated radio source to the observer.

We adopt two approaches to reduce the computational cost. The first is to trace only the ray paths detectable from the spacecraft trajectory (Approach 1). We define the intersection (the blue dotted line in Figure 2) of the initial ray path region (the red shade in Figure 2) and the plane including the observer, the icy moon center, and the radio source predicted by ExPRES (the gray shade in Figure 2). In the spherically symmetric ionosphere, radio waves are refracted in the radial direction away from the moon body. The radio waves emitted from the intersection are candidates for observable waves because they propagate on the plane (the blue solid lines in Figure 2). However, the radio waves from the other positions in the initial ray path region cannot be observed by the observer because they are refracted outward away from the plane (the red solid line in Figure 2). Thus, we can confine the ray paths to those from the intersection.

The second is to adopt a coordinate system defined by the initial wave number vectors (Approach 2). We set the coordinate system in the gray shaded area with the point on the icy moon surface closest to the ray path as the origin, the direction of the incident wave vector as the x-axis, and the vertical direction to the icy moon surface as the z-axis. We trace ray paths with the initial wavevectors parallel to the x-axis at 2 km intervals, as shown in Figure 3. These results can be replaced with the gray shaded area in Figure 2. The gray shading shifts depending on the position of the observer and the radio source predicted by ExPRES. However, the calculated ray paths in the shaded area do not change in the same spherically symmetric ionospheric model. Therefore, the ray tracing does not need to be repeatedly computed for each predicted radio source position.

Now, we consider the case of tracing ray paths emitted from the four types of radio source regions (A, B, C, and D) with an initial ray path region of 11,713 × 11,713 km. If the two approaches introduced in the previous paragraphs (Approaches 1 and 2) are not adopted, the total number of ray paths for each time step is approximately 1.3×10^8; however, if the two approaches are applied, the total number of ray paths becomes approximately 5.9×10^3, which reduces the computation time to approximately 1/23,000. In addition, the ray paths at different times do not need to be calculated for the ionosphere with the same maximum electron density n_{max} and the scale height h_{scale}. The

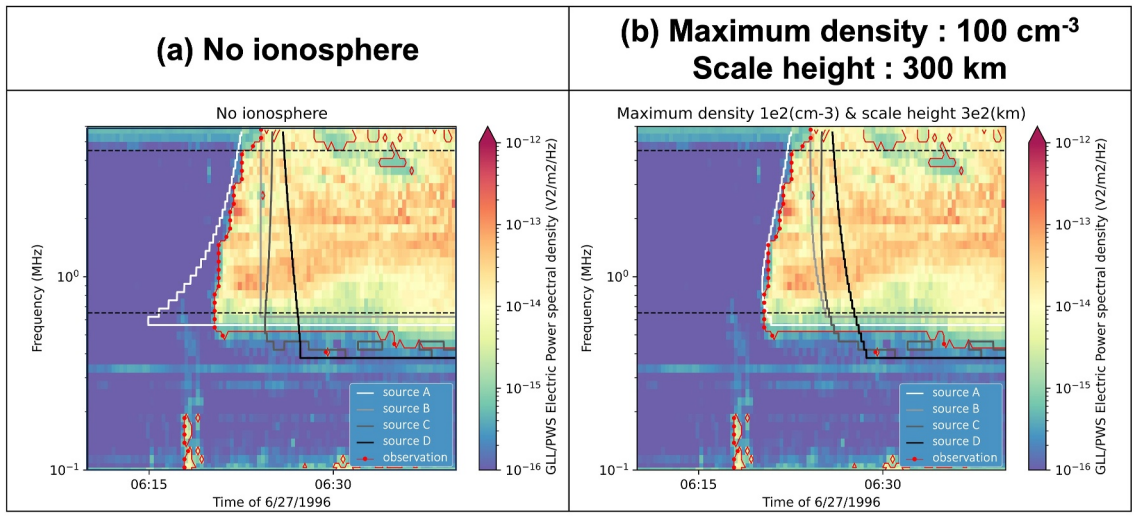

Figure 4. Superimposed GLL/PWS data and estimated Jovian radio emission occultation timing during the G01 flyby (f-t diagram). The four types of emission (A, B, C, D) are shown as the solid line in the white-to-black gradation. The observed occultation timings for each frequency derived from the GLL/PWS data are shown as the red dots on the solid lines. (a) Is for the case of no ionosphere, and (b) is for the case of the ionosphere with the maximum density of 100 cm^{-3} and the scale height of 300 km.

number of ray paths has a significant impact on the computation cost; so these two approaches were highly effective.

2.3. Estimation of the Maximum Electron Density, Scale Height, and Radio Source Type

With the maximum electron density, scale height, and types of radio source regions (A, B, C, and D), we fit our model with the observation results and evaluated the likelihood of fitting. To examine observed occultation time, we use the calibrated GLL/PWS LRS 152-channel data provided by the University of Iowa das2 server interface (Piker et al., 2019). The data are radio-electric power spectral densities provided in units of $V^2/m^2/Hz$, and the temporal resolution is 18.67 s. Figure 4 shows the power spectral densities as color maps at the end of occultation (egress) during the Ganymede 01 (G1) flyby. The occultation times for each radio source type, A, B, C, and D are shown as white, light gray, dark gray, and black solid lines, respectively. Figure 4a shows the simulation result assuming no ionosphere, while Figure 4b shows the results with an ionospheric maximum density of 100 cm^{-3} and a scale height of 300 km. In Figure 4b, the expected occultation time from source A matches the observation results better than that in the case without the ionosphere. The likelihood of fitting depends on the electron density distribution and radio source type. In the following, we explain the specific calculation method of the "average time difference."

To find the best-fit parameter of the ionospheric model, we introduce the "average time difference," which is a measure of the likelihood of fitting. The average time difference is the averaged time differences between the observed and modeled occultation start/end times for each frequency channel of the PWS. The observed occultation time is defined based on the observed power spectral densities compared to threshold values. The threshold values for each frequency are set at 10 times (10 dB) the average power density during the period when the Jovian radio emissions are occulted by the moons. This value corresponds to approximately three times (3σ) the standard deviation σ of the background electric field intensity (V/m) during occultation and can be used as an index of a significant enhancement in the radio intensity. The red frames in Figure 4 delimit radio waves exceeding the intensity threshold, which means that statistically significant Jupiter's radio waves are observed at the time and frequency in the red frames. We exclude the intense radio signals that are not continuous in time and frequency, such as low-frequency signals (<0.2 MHz) at approximately 06:18 in Figure 4, because they are assumed to be from sources other than auroral radio sources. The beginning (end) of the occultation in this examination is defined as the time when the observed radio intensity last (first) becomes above (below) the threshold.

The modeled occultation time is examined using the ray path model introduced in Section 2.2 and the spacecraft trajectory. The spacecraft trajectory data are computed by SPICE kernels (Acton, 1996) and retrieved using the

Table 2
Input Jovian Radio Source Types and Ionospheric Parameter Sets

Icy Moon	Ganymede	Callisto
Radio source type	A, B, C, D	
Maximum density (cm^{-3})	0, 12.5, 25, 50, 100, 150, 200 … (multiples of 50)	
Scale height (km)	25, 50, 100[a], 300, 600[a,b], 1000[c], 1,500	400, 600, 900

[a]cf. Eviatar, Strobel, et al. (2001). [b]Eviatar, Vasyliunas, and Gurnett (2001). [c]Gurnett et al. (1996).

NASA-JPL (Jet Propulsion Laboratory of the National Aeronautics and Space Administration) instance of WebGeoCalc (Acton et al., 2018). The trajectory data are linearly interpolated in time from the 1-min resolution data to the 1-s resolution data, as well as the ExPRES source position data. We place the spacecraft positions on the coordinate system of the gray plane in Figure 2 and examine when the modeled ray paths for each frequency become detectable (the white, light gray, dark gray, and solid black lines in Figure 4).

Frequency shifts during propagation due to the neutral atmosphere, plasma, and gravity of the Jovian magnetosphere and icy moons have a negligible effect on the refractive index. Therefore, the modeled frequencies can be assumed to remain unchanged. To match the frequency channels between the observed and modeled data, the modeled occultation times are logarithmically interpolated in frequency:

$$t_{int}\left(f_i\right) = \frac{log\left(\frac{f_i}{f_b}\right)}{log\left(\frac{f_a}{f_b}\right)}\left[t_{model}\left(f_a\right) - t_{model}\left(f_b\right)\right] + t_{model}\left(f_b\right) \tag{2}$$

where f_i is an observed frequency channel, f_a and f_b ($f_a \geq f_i \geq f_b$) are frequency channels modeled in ExPRES, t_{model} is the modeled occultation time, and $t_{int}(f_i)$ is the modeled occultation time interpolated at the observed frequency. We compare the observed occultation times $t_{obs}(f_i)$ at each frequency channel (the red line in Figure 4) with the interpolated occultation times $t_{int}(f_i)$. And calculate the time differences $|t_{obs}(f_i) - t_{int}(f_i)|$ for each frequency channel. In lower frequency channels (≤0.65 MHz), the time differences cannot be calculated for all four types of radio sources because both the modeled and observed occultation times cannot be defined. The higher frequency channels (≥4.5 MHz) have low sensitivity and a high noise floor. We calculate the average time differences T in the frequency channels between the black dashed lines in Figure 4 to disregard the frequency channels with these problems:

$$T = \frac{1}{n}\sum_{i}^{n}\left|t_{obs}\left(f_i\right) - t_{int}\left(f_i\right)\right| \tag{3}$$

We use this equation to calculate the average time differences $T(n_{max}, h_{scale})$ for each radio source types (A, B, C, and D), maximum ionospheric densities n_{max}, and ionospheric scale heights h_{scale} to find the best-fit parameter sets that have the lowest average time difference. The input parameters in this study are summarized in Table 2. Below 50 cm^{-3}, the inputs of the maximum density are 0, 12.5, 25, and 50 cm^{-3}. Above 50 cm^{-3}, the input densities are multiples of 50 cm^{-3} within the range where the smallest average time difference exists. The scale heights are between 25 and 1,500 km, including values referred to in several previous studies (Eviatar, Strobel, et al., 2001; Eviatar, Vasyliunas, & Gurnett, 2001; Gurnett et al., 1996).

3. Example of the Estimation Results

We provide an example of the modeling results that show the modeling sensitivity to the maximum density and scale height. We use an occultation event during the occultation egress during the Galileo G1 flyby.

Figures 5a–5c show examples of the observed frequency-time (f-t) diagrams with the modeled visibility, as shown in Figure 4. The red lines indicate the observed occultation times, and the white lines are the simulated occultation times for radio source A. Figures 5d–5f show the modeled Jovian radio ray paths, as in Figure 3; however, the radio frequency of the ray paths is 0.65 MHz, corresponding to the frequency indicated by the pink dashed line in

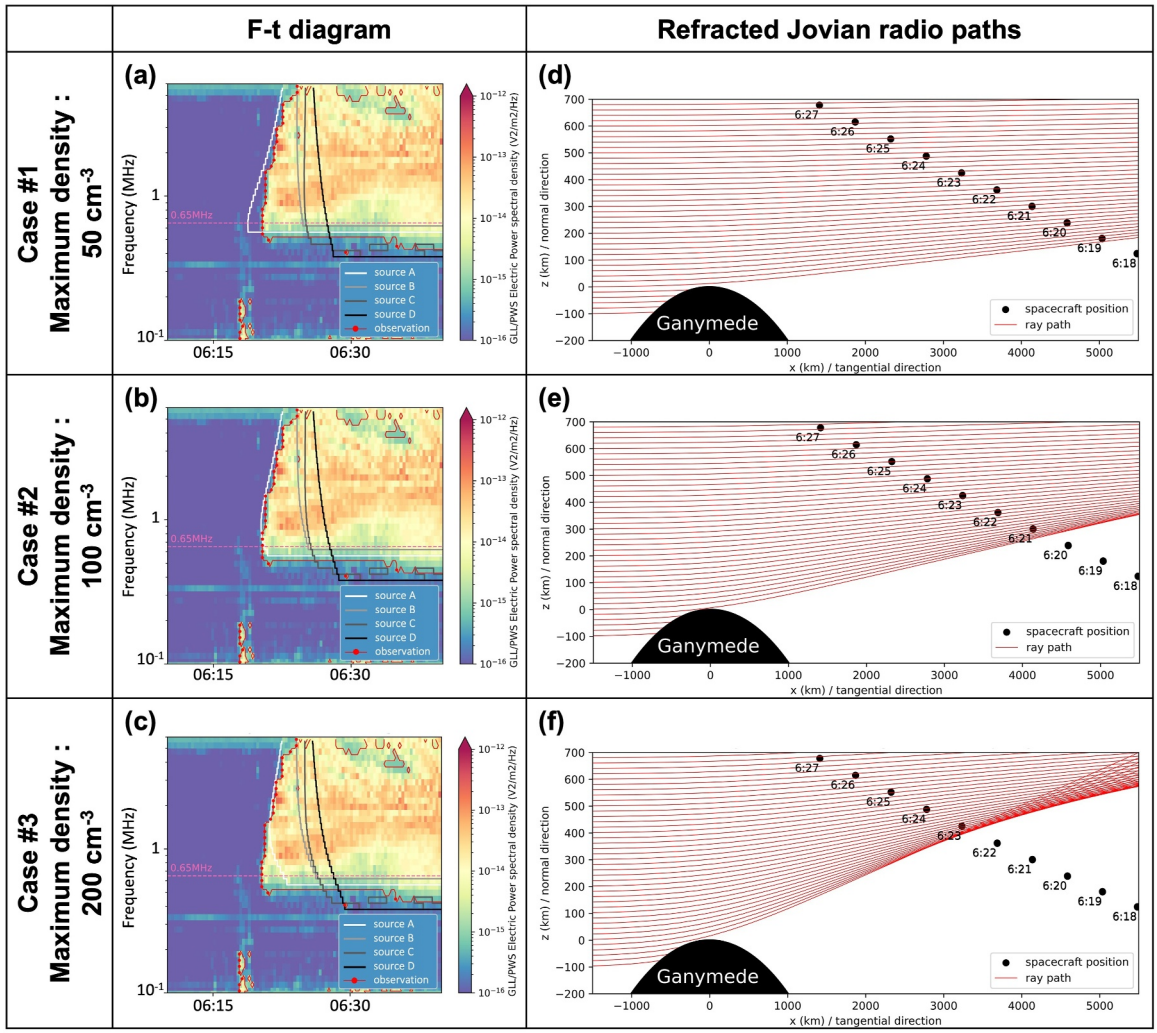

Figure 5. (a–c) Estimated Jovian radio emission occultation timing during the G01 flyby as Figure 4 and (d–f) Jovian radio paths at 0.65 MHz from the source A as Figure 3. In panels (d)–(f), the black dots indicate the position of the Galileo spacecraft at every minute. The ionospheric maximum density is 50 cm^{-3} in case #1 (a and d), 100 cm^{-3} in case #2 (b and e) and 200 cm^{-3} in case #3 (c and f). The scale height is the same at 300 km in all three cases.

Figures 5a–5c. We also plot the orbit of the Galileo spacecraft during the flyby at each minute. The ray paths are simulated with a scale height of 300 km and different maximum electron densities n_{max} of 50 cm^{-3} in Case #1 (Figures 5a and 5d), 100 cm^{-3} in Case #2 (Figures 5b and 5e), and 200 cm^{-3} in Case #3 (Figures 5c and 5f).

The observed occultation time (the red lines in Figures 5a–5c) of the radio at 0.65 MHz is at approximately 6:21. Figure 5d shows that Jovian radio waves are not greatly refracted due to the smaller maximum electron density (Case #1), and the radio wave detection starts at approximately 6:19. With a larger maximum electron density (Case #3), the radio waves are strongly refracted, and the radio wave detection starts at approximately 6:23 (Figure 5f). These results indicate that the ray paths with a higher electron density are more heavily refracted and greatly delay the end time of occultation compared to those with a lower electron density. For Case #1 (Figure 5a) and Case #3 (Figure 5c), the modeled occultation end times do not fit the observed times. With a middle value of maximum electron density (Case #2), the detections started at approximately 6:21 (Figure 5d), and the modeled time consistent with the observed time (Figure 5b). Thus, we can derive a unique maximum electron density for a constant scale height due to the correlation between the maximum electron density and the modeled occultation time.

Figure 6 shows the same events as Figure 5 but has a fixed maximum electron density of 100 cm^{-3} with different scale heights h_{scale}: 50 km in Case #4 (Figures 6a and 6d), 100 km in Case #5 (Figures 6b and 6e), and 1,000 km in

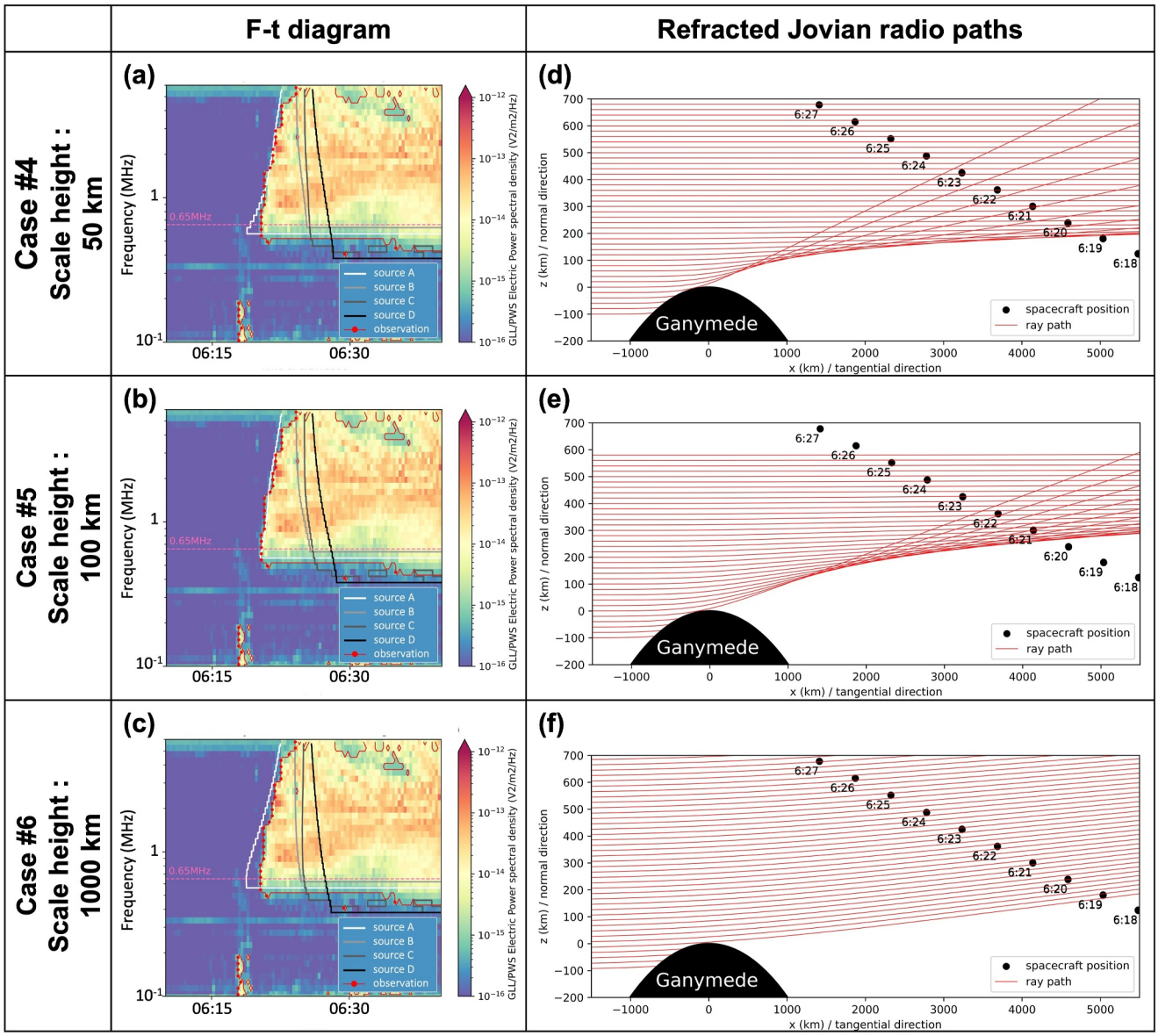

Figure 6. Estimated Jovian radio emission occultation timing during the G01 flyby and (d–f) Jovian radio paths at 0.65 MHz as well as the position of the Galileo spacecraft as Figure 5. The ionospheric scale height is 50 km in case #4 (a and d), 300 km in case #5 (b and e), and (c and f) 1,000 km. The ionospheric maximum density is the same at 100 cm^{-3} in all three cases.

Case #6 (Figures 6c and 6f). Figure 6d shows that Jovian radio waves are not refracted at a higher altitude (>200 km) with a smaller scale height ionosphere (Case #4). Figure 6f shows that radio waves are barely refracted even near the surface with a larger scale height ionosphere (Case #6). These radio waves begin to be detected at approximately 6:19 in Case #4 and Case #6, which are earlier than the observed occultation end time at 6:21. With a middle-scale height ionosphere (Case #5), the radio waves are refracted at any altitude, which leads to the latest occultation end time among these three cases and the modeled time fits the observed time (Figure 6b). Thus, the modeled occultation time also depends on the scale height, and we can derive a scale height for a constant maximum density.

Figure 7 shows the average time differences extended to all parameters listed in Table 1. The vertical and horizontal axes show the scale height and the maximum electron density, respectively. The color bar shows the average time differences (in seconds). The star indicates the best-fit parameter with the minimum average time difference. The contour lines indicate the average time differences interpolated by cubic spline interpolation using

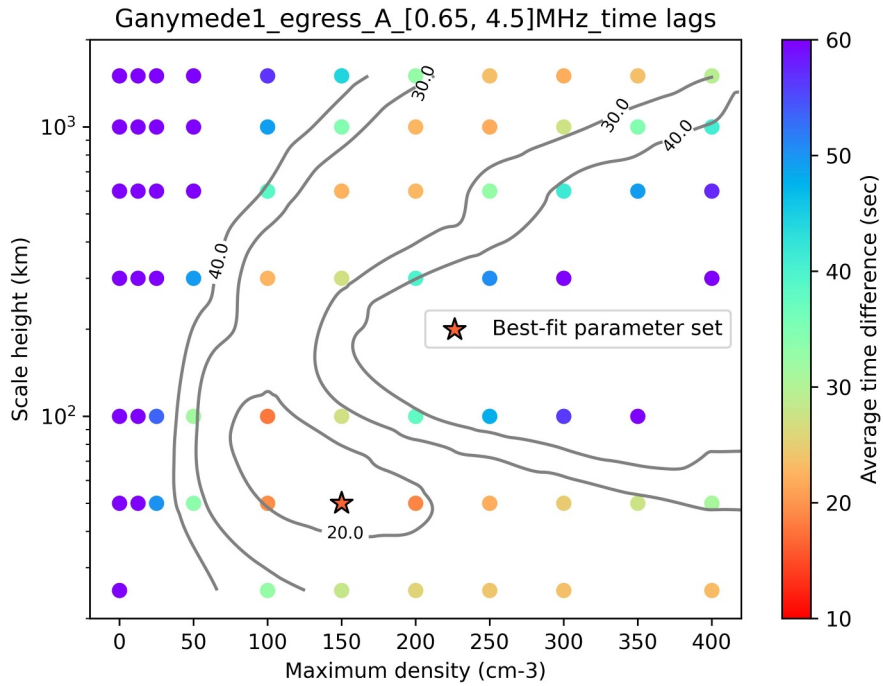

Figure 7. Average time differences between the observed occultation timings and the expected timing during the G1 flyby. The vertical axis represents the ionospheric scale height, and the horizontal axis represents the maximum electron density. The star indicates the best-fit ionospheric parameter set, which has the smallest average time difference. The contour lines indicate the average time differences interpolated by cubic spline interpolation. The radio source type A is assumed here.

the interpolate module in the scipy.py library. The best-fit parameter set has a maximum electron density of 150 cm^{-3} and a scale height of 50 km. Focusing on the parameter sets with time differences less than 25 s (orange and yellow dots), the maximum density is effectively constrained from 100 to 350 cm^{-3}. The orange and yellow dots are spread over a wide scale height range of 50–1,500 km presenting the difficulty in constraining the scale height by this method. In Section 4, we show both the best-fit parameter set and the color map of average time differences (plotted as in Figure 7). The best-fit parameter set is the maximum likelihood case for the ionospheric density; however, a greater uncertainty is observed in the scale height than the maximum density, as shown in the color maps.

4. Results

The following criteria is used to exclude the radio data for the sake of precision in deriving the occultation timing: (a) the noise observed during occultation was large (e.g., egress during the Callisto 30 (C30) flyby; see Figure 5 of Cecconi et al. (2021)); (b) all radio waves from the four source types were not occulted (e.g., the Ganymede 07 flyby; see Figure 10 of Cecconi et al. (2021)); and (c) the observed Jovian radio waves were weak (e.g., the Europa 12 flyby, see Figure 6 of Cecconi et al. (2021)). We have clear occultation events, and these events are not found in one of the 3 criteria: for only two events with Ganymede (the occultation ingress and egress during the G01 flyby) and two events with Callisto (the occultation egress during the Callisto 9 (C9) flyby and the occultation ingress during the Callisto 30 flyby).

4.1. Ganymede Ionosphere

The G1 flyby had the closest approach of 835 km to Ganymede at 6:29 UT on 27 June 1996. Around that moment, the Jovian radio waves started to be occulted when the spacecraft was on Ganymede's trailing side (ingress), and then the occultation ended when the spacecraft was on the leading side (egress). Our modeling results are shown in Figures 8a, 8c, and 8e for the ingress and Figures 8b, 8d, and 8f for the egress.

Figure 8a shows the observed f-t diagrams during ingress with the modeled visibility assuming no ionosphere in the same format as in Figure 4. The modeled occultation time for radio source type B (the light gray line in

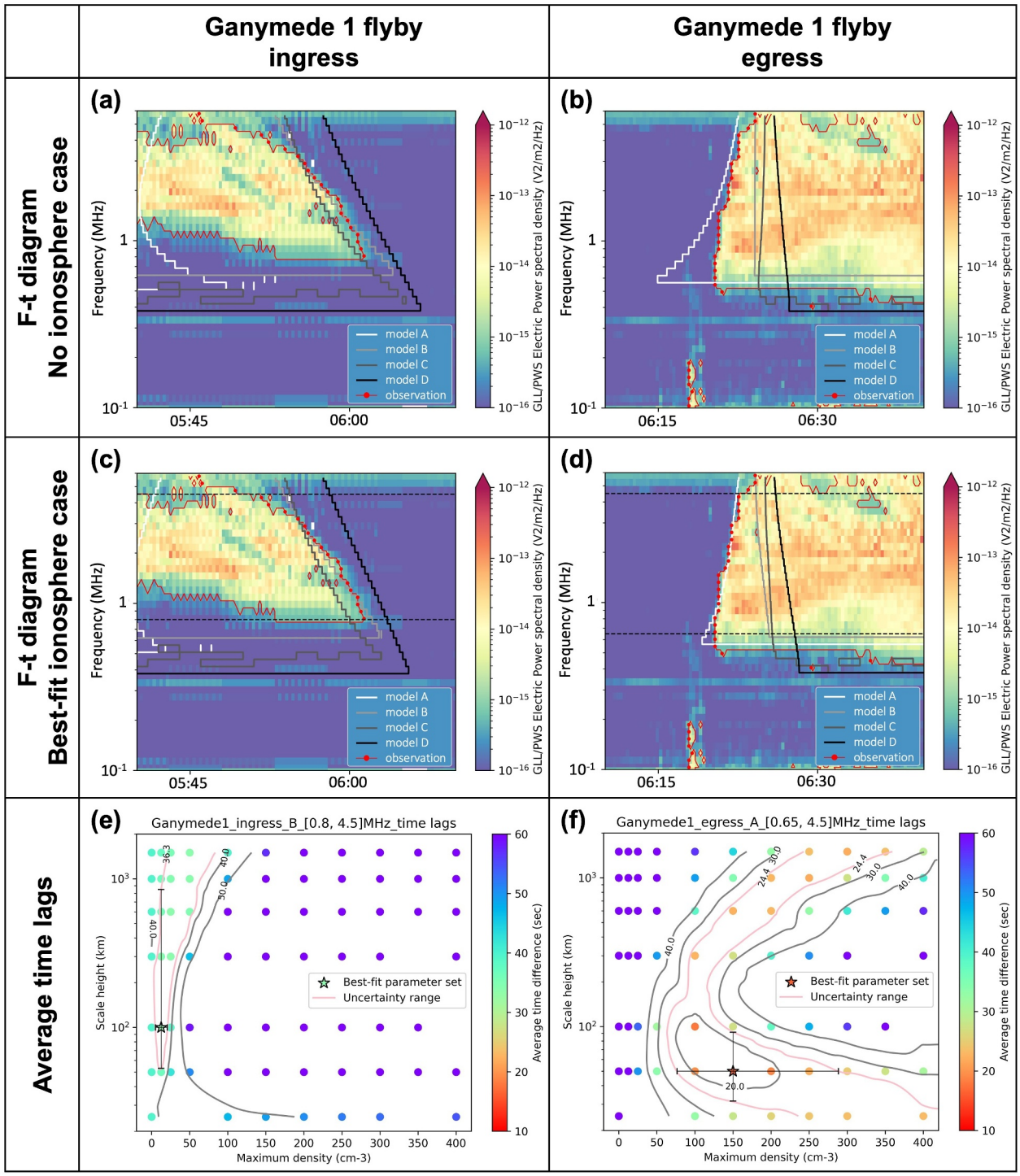

Figure 8. (a–d) Superimposed GLL/PWS data and estimated Jovian radio emission occultation as Figure 4 and (e and f) average time differences for some cases of ionospheric parameter set as Figure 7. The rows represent two application cases for Ganymede ionosphere (Ganymede G1 flyby ingress and egress). (a and b) Are for the case of no ionosphere. (c and d) Are for the case of ionospheres with the best-fit parameter set. The error bars in figures (e) and (f) indicate the uncertainties of maximum density and scale height for the best-fit parameter set.

Figure 8a) fits well with the observed time (the red line in Figure 8a), especially at 1–3.5 MHz. However, above 3.5 MHz and below 1 MHz, the modeled occultation time occurred later than the observed occultation time by more than 50 s. For this case, the average time difference was estimated to be 39.3 s for the 0.8–4.5 MHz channel;

this channel is selected based on the criteria noted in Section 2.3 (between the dashed black line in Figure 8b). We also calculated the average temporal differences by changing the radio source types and ionospheric parameter sets. Figure 8e shows the average temporal differences for radio source B as a function of the ionospheric maximum density and scale height in the same format as in Figure 7. We found that the best-fit case had a maximum electron density of 12.5 cm^{-3}, a scale height of 100 km, and a type B radio source. The corresponding average time difference was 33.6 s. The corresponding average time difference was the smallest of all radio source types. The f-t diagram with this parameter set case (Figure 8c) showed that the model fitting to the observed time was improved more than Figure 8a, and the time difference became less than 40 s even below 1 MHz.

Figures 8b, 8d, and 8f are the same as Figures 8a, 8c, and 8e but for an egress part in the flyby. The f-t diagram for the no ionosphere case (Figure 8b) showed that the modeled occultation time for source type A (the white line in Figure 8b) was earlier than the observed time (the red line in Figure 8b), especially below 2 MHz, by up to approximately 5 min. The average time difference was estimated to be 83.0 s for the 0.65–4.5 MHz channels based on the same criteria as in the ingress case. We calculated the average temporal difference as a function of the ionospheric maximum density and scale height, as shown in Figure 8f. As a result, we found that the best-fit parameter case had a maximum electron density of 150 cm^{-3}, a scale height of 50 km, and type A radio source. The average time difference was 16.5 s. The f-t diagram for the best-fit parameter set (Figure 8d) showed that the modeled time fit the observed time better than Figure 8b, and the time difference became less than 50 s even below 2 MHz.

4.2. Callisto Ionosphere

The closest approach of 418 km to Callisto during the C9 flyby was at 13:48 UT on 25 June 1997, and that of 138 km during the C30 flyby was at 11:23 UT on 25 May 2001. Our modeling results are shown in Figures 9a, 9c, and 9e for the egress during the C9 flyby and in Figures 9b, 9d, and 9f for the ingress during the C30 flyby.

Figures 9a, 9c, and 9e are in the same format as Figures 8a, 8c, and 8e but show the results for the egress in the C9 flyby. The f-t diagram for the no ionosphere case (Figure 9a) showed that the modeled time for source type D (the black line in Figure 9a) fit the observed time only above 1 MHz. However, below 1 MHz, the modeled occultation time was earlier than the observed occultation time by more than 160 s. In this case, the average time difference was estimated to be 75.8 s Figure 9e shows the average time differences for the source of type D. We found that the best-fit case had a maximum electron density of 350 cm^{-3}, a scale height of 400 km, and a radio source of type D. The average time difference for this best-fit case was estimated to be 34.1 s. The f-t diagram (Figure 9c) showed that the modeled occultation time (the black line in Figure 9c) was delayed, and the time differences became less than 50 s below 1 MHz. The f-t diagram for ingress during C30 flyby with no ionosphere (Figure 9b) showed that the modeled times effectively fit the observed occultation time with any type of radio source ($\leq$14.7 s). Especially for the radio source of type C, the time differences were less than 21 s below 2 MHz, and the fits were good. In this case, the average time difference was estimated to be 9.8 s Figure 9f shows the average time differences for source type C. The average time differences were small with a smaller electron density. The best-fit case was found to have a maximum electron density of 12.5 cm^{-3}, a scale height of 400 and 600 km, and radio source type C. The average time difference in the best-fit case was 9.6 s, which was only 0.2 s shorter than that with no ionosphere. A comparison of the f-t diagrams (Figures 9b and 9d) showed that the modeled occultation time (dark gray line) did not drastically change between the no ionosphere and best-fit cases. These results indicated that the icy moon ionosphere did not affect the ray path in this case.

5. Discussion

5.1. Average Time Difference and Uncertainty of Occultation Timing

We showed the minimum average time difference with the best-fit parameter set for each occultation event. The smallest average time difference for occultation ingress in the C30 flyby was 9.6 s, and this value was the smallest in all events. However, the minimum average time differences for egress during the C9 flyby and ingress during the G1 flyby ingress were greater, with values of 33.6 and 34.1 s, respectively; these values were more than three times greater than that for ingress during the C30 flyby. The larger minimum average time differences could be explained by the following reasons.

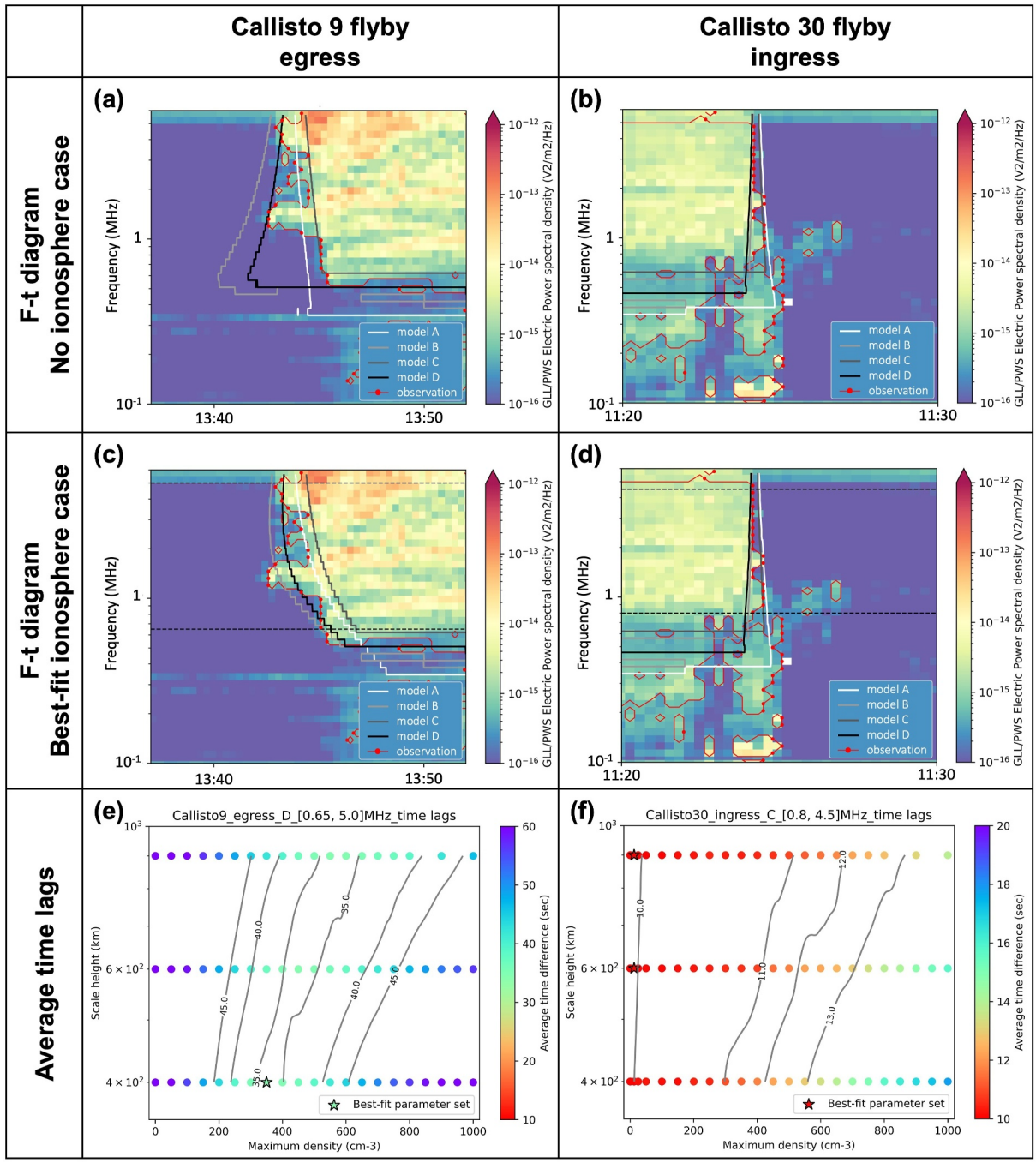

Figure 9. The same frequency-time diagrams and average time differences as Figure 8 but for two application cases for Callisto ionosphere (Callisto C9 flyby egress and Callisto C30 flyby ingress).

1. The uncertainty of the radio source position in the ExPRES model resulted in uncertainty in the modeled occultation time (Table 2 of Cecconi et al. (2021)).
2. The time step of the Galileo PWS observation $\delta\tau$ (18.67 s) caused uncertainty in the observed occultation time (Gurnett et al., 1992).
3. Since the actual ionosphere has the temporal and spatial variation of scale heights and maximum electron densities, the occultation time modeled with a single unique ionospheric parameter was difficult to fit with the observed time.

Table 3
Temporal Uncertainty of the Time Differences Between the Observed Occultation Timings and the Expected Timing

	Standard temporally uncertainty (sec)					
	Radio source position $u_1(f_i)$					
Flyby	800 kHz	1 MHz	2 MHz	4 MHz	PWS time step u_2	Combined $\overline{u}$
G01 ingress	47.7	43.5	34.8	26.0	5.4	36.3
G01 egress	46.6	32.7	14.5	7.7		24.4
C09 egress	13.2	10.9	6.2	3.9		9.7
C30 ingress	2.0	1.6	1.2	0.6		5.5

4. The observed occultation time was shifted due to the reflection effects of Jovian radio waves in the Jovian magnetosphere (Gurnett et al., 1998; Menietti et al., 2003); this effect was not considered in our model.

The time differences noted by the reason 3 and 4 were depended on the variation of icy moon ionosphere and Jovian magnetosphere at the time of the flyby. Therefore, uncertainties of modeled occultation timing due to these two reasons difficult to be defined. In this paper, we focus on the uncertainties by the reason 1 and 2 and propose the "standard uncertainty" referred in European Accreditation (2022). The standard uncertainty $\boldsymbol{u}_1(\boldsymbol{f_i})$ of the modeled occultation timing due to the reason 1 is calculated as follows:

$$u_1\left(f_i\right) = \frac{\delta t(f_i)}{2\sqrt{3}} \tag{4}$$

where f_i is an observed frequency at a channel i, and $\delta t(f_i)$ is the possible range of modeled occultation timing calculated with the spacecraft trajectory data and the angular uncertainty of Jovian radio sources location (Table 2 of Cecconi et al. (2021)). With the same approach, we also calculate the standard uncertainty u_2 of the observed occultation timing due to the reason 2 as follows:

$$u_2 = \frac{\delta\tau}{2\sqrt{3}} \tag{5}$$

where $\delta\tau$ is the time step of the Galileo PWS observation. The averaged value $\overline{\boldsymbol{u}}$ of the combined standard uncertainty of the two standard uncertainties, $u_1(f_i)$, and u_2, is calculated as follows:

$$\overline{u} = \frac{1}{n}\sum_{i}^{n}\sqrt{u_1\left(f_i\right)^2 + {u_2}^2} \tag{6}$$

Table 3 shows each standard temporary uncertainty $u_1(f_i)$ and u_2, as well as the averaged value of the combined standard uncertainty $\overline{u}$ for each occultation event. For ingress and egress during the G1 flyby, the uncertainties due to the source locations are significant, yielding considerable average values of the combined standard uncertainty. On the other hand, for ingress during the C30 flyby, the uncertainties from the source positions are small, and the average of combined standard uncertainty is also small. These variations of uncertainty for each occultation event are consistent with the uncertainty trend in Cecconi et al. (2021).

Figures 8e and 8f show the parameter ranges where the average time differences become the average of combined standard uncertainty with the red line for the G1 flyby. The figures also show the uncertainties of the maximum density and scale height for the best-fit parameter set with error bars. The uncertainty of the scale height ranges from 53.0 to 846.5 km for the ingress and from 31.5 to 91.5 km for the egress. This significant uncertainty in the results for the ingress is due to the weak constraints on the scale height of our method, which are also mentioned in Section 3. On the other hand, the maximum electron density ranges from 5.0 to 20.5 cm^{-3} for the ingress and from 76.5 to 288.5 cm^{-3} for the egress. We found that our method imposes tight constraints on the maximum electron density. In the following discussion of Ganymede ionosphere, we will focus on the maximum electron density with the minimum time difference and the uncertainty.

For the results of the egress in the C9 flyby and the ingress in the C30 flyby, we cannot indicate uncertainties of the maximum density and scale height because the minimum average time difference is larger than the average of combined temporary standard uncertainty. The significance of the minimum average time difference should be attributed to factors other than reasons 1 and 2. Some ionospheric models predicted that the ionosphere of icy moons has a spatial density variation and spherical asymmetry (Carnielli et al., 2019). Thus, there is some uncertainty due to reason 3. The suggested best parameter set in this study represents the averaged electron density distribution of the ionosphere with spatial variation. In the following discussion for Callisto, we will focus only on the best-fit parameter set with the minimum time difference.

5.2. Density Distributions and Formation Processes

The ionized atmosphere of icy moon is produced through the atmospheric supply and ionization of atmospheric neutrals as described in the introduction. These processes are attributed to Jovian magnetospheric plasma precipitation and solar illumination effects. We investigated the maximum electron density and observation points in our study and previous observations to assess the plasma and solar effects.

According to our results for the Ganymede ionosphere, the maximum ionospheric density for egress during the G1 flyby was from 76.5 to 288.5 cm^{-3}, whereas that for ingress was from 5.0 to 20.5 cm^{-3}. The observation point is defined as the nearest point on the moon's surface from the straight line connecting Jovian radio sources and the spacecraft before/after the occultations. For the results from the previous radio science observations, we examined all maximum electron density values reported in published papers (Buccino et al., 2022; Kliore, 1998). We defined the observation point as the tangential point on the moon's surface to the line connecting the earth (the observer) and the spacecraft. For the results from the previous in situ observations, we used all electron density profiles reported in the published papers (Eviatar, Strobel, et al., 2001; Eviatar, Vasyliunas, & Gurnett, 2001; Gurnett et al., 1996). The maximum density was the density at the moon surface according to extrapolation from the density profiles, and the observation point was the point just below the spacecraft closest to the ice moons. We noted that these observation points were rederived from the trajectory data of SPICE WebGeoCalc (Acton et al., 2018) and differed from the observation points assumed in previous papers.

The solar illumination effect is organized by the solar zenith angle (SZA); the SZA is the angle between the subsolar and observation points. Figure 10a shows the maximum electron density determined by our Jovian radio occultation observation (square), previous radio science observation (star), and in situ observation (circle) as a function of the SZA. The electron density in the lower SZA region ($\leq$80°) was lower than that in the higher SZA region (>80°). Our derived density on the day side (egress) was also lower than most of the densities obtained by previous observations in the higher SZA region. No clear trend of atmospheric ionization by solar illumination was observed from the results of previous observations and the results from our study.

Ganymede's intrinsic magnetic field creates a closed field and prevents plasma access to the closed field (Liuzzo et al., 2020; Poppe et al., 2018). Charged particles in the Jovian magnetosphere therefore precipitate mainly in the region where the field lines are connected to the Jovian magnetic field. Figure 11 shows the maximum electron density map on Ganymede's surface for previous observations and our results. The location (longitude, latitude) of (0°W, 0°) is roughly toward Jupiter's center, and that of (270°W, 0°) is roughly the trailing hemispheric center. The location of the open/closed field line (OCFL) boundary has been noted by several studies (Khurana et al., 2007; Kopp & Ip, 2002; Jia et al., 2008, 2009; McGrath et al., 2013) and depends on the modeling method and assumed plasma sheet location. Based on these OFCL boundary models, we outline the region where the OCFL boundaries lie (boundary region) with the dashed line in Figure 11. The G1 ingress observation points (5.0–20.5 cm^{-3}) are at approximately 270°W longitude with latitudes of 12°N–39°N. Most of the observation points are at lower latitudes than the OCFL boundary region. The G1 egress observation points (76.5–288.5 cm^{-3}) are at approximately 80°W longitude with latitudes of 39°N–51N°, and the points are in the open magnetic field line regions. Our derived electron density is greater in the open magnetic field line regions than in the closed field line region. According to previous observation results, the observation point of the radio science at a longitude of 38°W and a latitude of 20° is in the closed field line region. However, the in situ observation points at approximately 85°W longitude and 75° latitude and the other radio science observation points are in the open field line region. We found that the results from these previous observations produced the same trend as our results; the electron density was greater in the open magnetic field line regions than in the closed field line region.

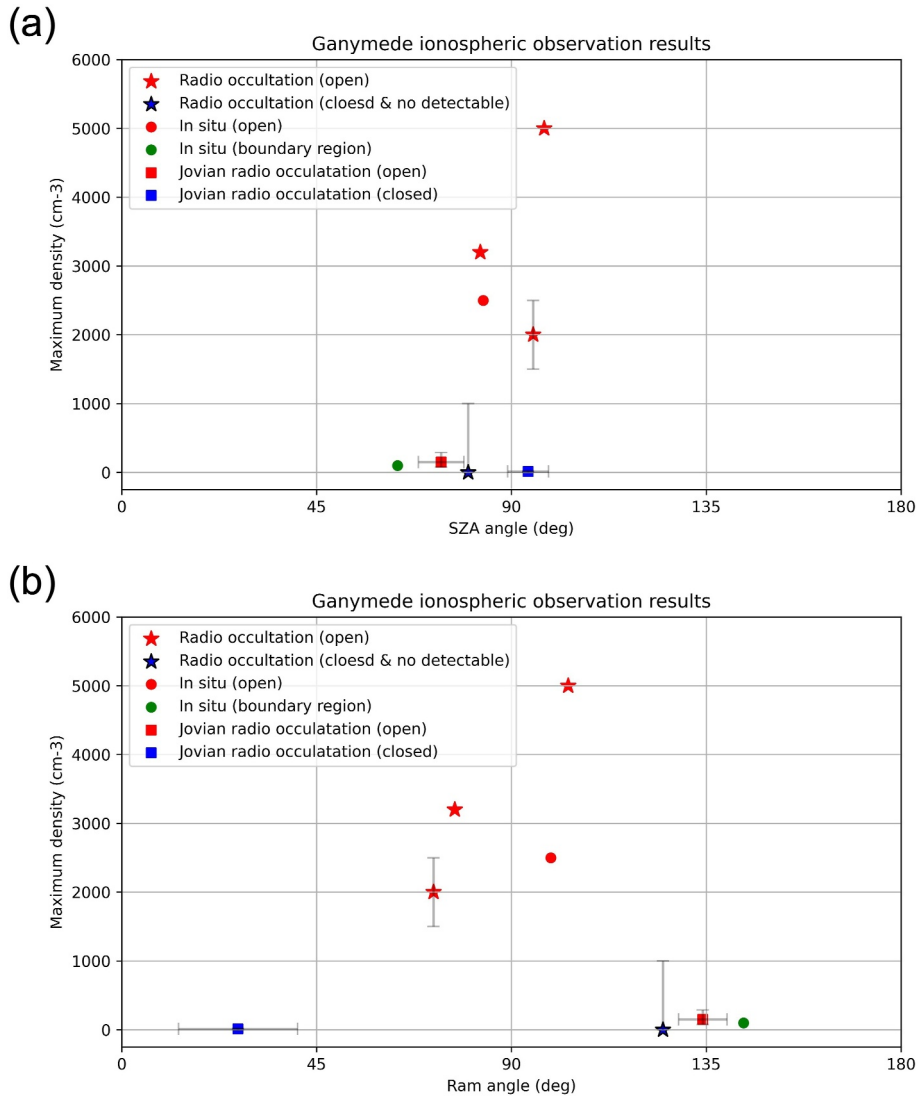

Figure 10. Maximum electron density in Ganymede's ionosphere observed with the previous radio occultation observations (star), in situ observation (circle), and our Jovian radio occultation observations (square). Each color represents whether the observation points are in an open magnetic field region (red), a closed magnetic field region (blue), or a boundary region between open and closed field regions (green). Panel (a) shows the electron density as a function of the SZA (solar zenith angle) of the observation points. Panel (b) shows the density as a function of the ram angle, the angle between trailing center direction and observation points.

The plasma precipitation is also connected to the ram angle; the ram angle is the angle between the trailing center direction (270°W, 0°) and the observation point. Poppe et al. (2018) and Liuzzo et al. (2020) presented a thermal and energetic ion precipitation map and an energetic electron map. These precipitation models indicated regional differences in the plasma precipitation flux. The flux was larger in regions. The flux in the open magnetic field line was greater in the region with lower ram angles. Figure 10b shows the maximum electron density as a function of the ram angle. All observational results in the closed magnetic field line regions (the blue plots), including our G01 ingress results, had a lower maximum electron density than those in the open magnetic field line regions (the red plots). Focusing on the open magnetic field line region, the density at lower ram angles (<120°) was greater than that at higher ram angles (>120°). Based on the above discussion, we assumed that the observed density distribution was correlated with the flux distribution of plasma precipitation from the Jovian magnetosphere.

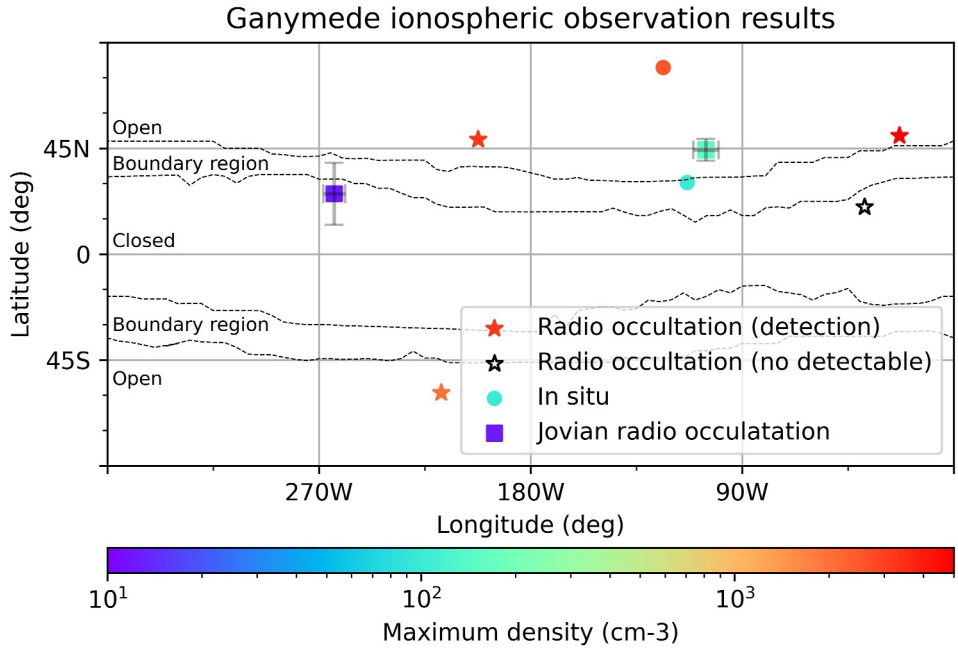

Figure 11. Maximum electron density of Ganymede's ionosphere with the observation point. Observation methods are classified with the same shapes as Figure 10. Each color represents the maximum density in the color bar. The vertical axis represents the observation point's latitude, and the horizontal axis represents the observation point's longitude. The dashed line outlines the region where OCFL boundaries lie suggested in previous papers (boundary region). The leading hemisphere extends from 0°W to 180°W and the trailing hemisphere extends from 180°W to 360°W.

The correlation between the electron density and the plasma flux can be explained by several atmospheric model studies in Ganymede. Vorburger et al. (2022) modeled the sublimated and sputtered H_2O exospheres of Ganymede. They indicated that sublimated exospheres were dominant up to 60° SZA, while sputtering atmospheric production was dominant elsewhere. As shown in Figure 10a, all observations were collected in a region where the SZA exceeded 60°. The neutral atmospheric density at these observation points was likely controlled by the precipitation plasma flux from the Jovian magnetosphere. Carnielli et al. (2019) modeled the 3D electron density distribution of the Ganymede ionosphere produced by electron impact ionization and photoionization. Using the model assumptions, they found that the rate of electron impact ionization in the open field line region was 0.19×10^{-8}–9.05×10^{-8} s^{-1} and greater than the photoionization rate on the day side (0.01×10^{-8}–1.75×10^{-8} s^{-1}). The effective electron impact mainly contributed to the ionization of the sputtered atmosphere. According to these studies, sputtering atmospheric production and electron-impact ionization led to an electron density distribution correlating with the plasma flux.

For the Callisto ionosphere, we found a maximum electron density of approximately 350 cm^{-3} for the C9 egress and approximately 12.5 cm^{-3} for the C30 ingress. Figure 12a shows the maximum electron density as a function of the SZA. The SZAs were 171.3°–176.3° for C9 egress (night side) and 103.9°–105.4° for C30 ingress (night side). Figure 12a also shows the maximum electron density observed by the previous science results (Kliore et al., 2002). Most observation results around the day-night terminator derived from the previous science were greater than those derived by our method. The observed density tended to be higher with lower SZA. The plasma precipitation flux to Callisto is simply organized by the ram angles because Callisto has no intrinsic magnetic field. Figure 12b shows the maximum electron density as a function of the ram angles. The ram angles of our results were 1.8°–7.4° for C9 egress (trailing hemisphere) and 165.9°–167.2° for C30 ingress (leading hemisphere). Even with smaller ram angles, the observed electron densities were not high. We found that Callisto's ionosphere was affected by solar illumination rather than by the plasma precipitation.

These characteristics of Callisto's ionosphere are consistent with the Callisto exospheric model in Vorburger et al. (2015). They modeled the atmospheric density profiles at the subsolar point and the antisolar point, that were generated through sputtering and sublimation of the surface. They indicate that the sublimated atmosphere at the

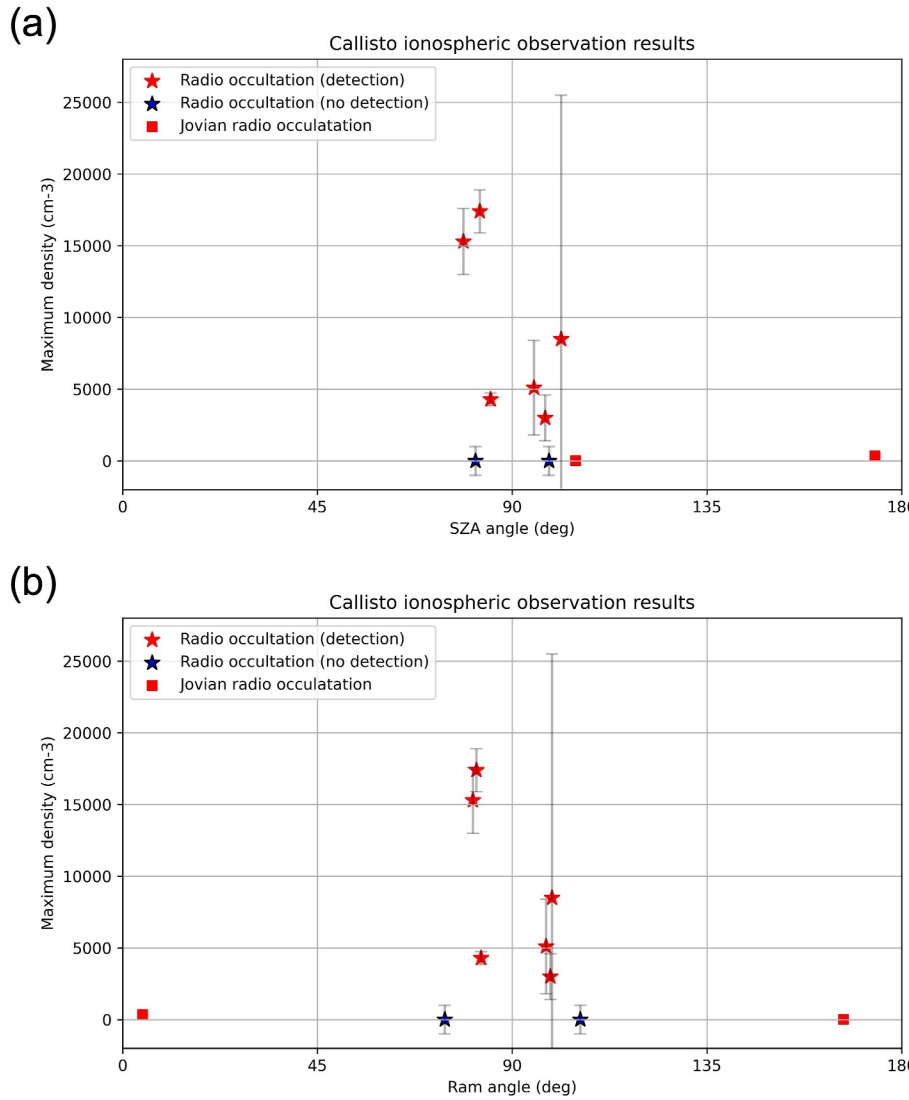

Figure 12. Observed maximum electron density in Callisto's ionosphere shown with the previous radio occultation observations (star) and our Jovian radio occultation observations (square). Each color represents whether there is detectable ionosphere (red) or not (blue). Panel (a) shows the electron density as a function of the SZA of the observation points. Panel (b) shows the density as a function of the ram angle, the angle between trailing center direction and observation points.

subsolar point was denser than that at the antisolar point. The sublimated atmosphere at the subsolar point was approximately 10^8 times denser than the sputtering atmosphere. These results indicate that sublimation on the day side is the main process that produces the neutral atmosphere on Callisto. In their study, the two main ionization processes, photoionization, and electron-impact ionization, are assumed to be the exospheric loss processes. They indicated that the photoionization rate (10^{-8}–10^{-10} s^{-1}) was as large as the electron-impact ionization rate (10^{-9} s^{-1}) (Huebner et al., 1992; Vorburger et al., 2015). The photoionization of the dense sublimated atmosphere on the day side led to the characteristics of the observed density distribution in Callisto.

We found difference in the controlling process between Ganymede's and Callisto's ionospheric structures. One cause of these differences was the density of Jovian magnetospheric plasma near each moon. While the solar fluxes at these moons are the same because of the same average distance from the Sun, the Jovian magnetospheric electron density at Ganymede was 1–10 cm^{-3} and higher than that at Callisto (0.01–0.70 cm^{-3}) (Kivelson et al., 2004). The denser magnetospheric plasma at Ganymede likely enhanced the dependency of the ionospheric density on the precipitation plasma flux. The few observations shown in Figures 10 and 12 cannot simply explained by the SZA or ram angles; the results showed a dense ionosphere (5,000/cc) with an approximately

100° ram angle at Ganymede and a thin ionosphere (no detection) with an approximately 80° SZA at Callisto. Some possible reasons for the unexplained observations may be regional differences in local plasma precipitation (Liuzzo et al., 2020; Poppe et al., 2018) or differences in the surface temperature between the dawn and dusk sides (Leblanc et al., 2017). Surface compositions are also thought to vary in different regions and can change the neutral atmospheric density (Vorburger et al., 2015). The observation results discussed here likely include the effects of these regional differences in the ionospheric structure.

6. Conclusions

In this study, we developed new ionospheric occultation observations using Jovian radio waves, which enabled observations over a wide range of solar phase angles and at low altitudes based on Cecconi et al. (2021). We adopted this approach to investigate the electron density distribution and formation mechanism of the icy moon ionospheres.

Our analysis of Ganymede's ionosphere during the Galileo G1 flyby revealed that the maximum electron density was 5.0–20.5 cm^{-3} in the closed magnetic field region and 76.5–288.5 cm^{-3} in the open magnetic field region. The density difference between the closed and open field regions was consistent with previous radio science and in situ observation results and indicated that plasma precipitation promoted ionized atmosphere production through surface material sputtering and/or electron-impact ionization of atmospheric neutral species. For Callisto's ionosphere, we found that the maximum density was approximately 350 cm^{-3} during the C9 flyby and 12.5 cm^{-3} during the C30 flyby. The data for these two results from Calisto's ionosphere originated from the night side of the ionosphere, and the determined densities were lower than most of the previous observation results around the day-night terminator. These results were consistent with the models previously studied, indicating that sublimation dominated atmospheric production.

Our results provide insight into the atmospheric supply and ionization in Ganymede and Callisto. We plan to apply our method to the upcoming JUICE/Radio and Plasma Wave Investigations data. Future studies will provide a broad view of the detailed structure of the icy moon ionospheres and their possible generation processes.

Data Availability Statement

All simulation codes used for this study are available at the following GitHub repository (https://github.com/rikuto-yasuda/icymoon_raytracing) and Zenodo repository (Yasuda et al., 2024). The product from Jovian radio source modeling results used in this study are available at https://doi.org/10.25935/8zff-nx36 (Cecconi et al., 2022). The calibrated GLL/PWS LRS data (Gurnett, Kurth, & Granroth, 1997) used in our research are available on the University of Iowa das2 server interface (Piker et al., 2019) at http://das2.org/browse/uiowa/galileo/pws/survey_electric.

Acknowledgments
This research was supported by the International Joint Graduate Program in Earth and Environmental Sciences, Tohoku University (GP-EES). This research was supported by Grant-in-Aid for JSPS Fellows (Grant 23KJ0166). Tomoki Kimura was supported by Grants-in-Aid for Scientific Research KAKENHI (Grants 20H01956 and 19H05184) from the Japan Society for the Promotion of Science (JSPS). Fuminori Tsuchiya was supported by JSPS KAKENHI (Grant 20KK0074).

References

Acton, C., Bachman, N., Semenov, B., & Wright, E. (2018). A look towards the future in the handling of space science mission geometry. *Planetary and Space Science*, *150*, 9–12. https://doi.org/10.1016/J.PSS.2017.02.013

Acton, C. H. (1996). Ancillary data services of NASA's navigation and ancillary information facility. *Planetary and Space Science*, *44*(1), 65–70. https://doi.org/10.1016/0032-0633(95)00107-7

Arnold, H., Liuzzo, L., & Simon, S. (2020). Plasma interaction signatures of plumes at Europa. *Journal of Geophysical Research: Space Physics*, *125*(1), e2019JA027346. https://doi.org/10.1029/2019JA027346

Buccino, D. R., Parisi, M., Gramigna, E., Gomez-Casajus, L., Tortora, P., Zannoni, M., et al. (2022). Ganymede's ionosphere observed by a dual-frequency radio occultation with Juno. *Geophysical Research Letters*, *49*(23), e2022GL098420. https://doi.org/10.1029/2022GL098420

Carnielli, G., Galand, M., Leblanc, F., Leclercq, L., Modolo, R., Beth, A., et al. (2019). First 3D test particle model of Ganymede's ionosphere. *Icarus*, *330*, 42–59. https://doi.org/10.1016/J.ICARUS.2019.04.016

Cecconi, B., Louis, C. K., Muñoz, C., & Vallat, C. (2022). Jovian auroral radio source occultation modeling and application to the JUICE science mission planning. Supplementary Material: Galileo Flybys [Dataset]. *PADC/MASER*. https://doi.org/10.25935/8zff-nx36

Cecconi, B., Louis, C. K., Muñoz Crego, C., & Vallat, C. (2021). Jovian auroral radio source occultation modelling and application to the JUICE science mission planning. *Planetary and Space Science*, *209*, 105344. https://doi.org/10.1016/J.PSS.2021.105344

Connerney, J. E. P., Kotsiaros, S., Oliversen, R. J., Espley, J. R., Joergensen, J. L., Joergensen, P. S., et al. (2018). A new model of Jupiter's magnetic field from Juno's first nine orbits. *Geophysical Research Letters*, *45*(6), 2590–2596. https://doi.org/10.1002/2018GL077312

European Accreditation. (2022). Evaluation of the uncertainty of measurement in calibration. Retrieved from https://european-accreditation.org/publications/ea-4-02-m/

Eviatar, A., Strobel, D. F., Wolven, B. C., Feldman, P. D., Mcgrath, M. A., & Williams, D. J. (2001). Excitation of the Ganymede ultraviolet aurora. *The Astrophysical Journal*, *555*(2), 1013–1019. https://doi.org/10.1086/321510

Eviatar, A., Vasyliunas, V. M., & Gurnett, D. A. (2001). The ionosphere of Ganymede. *Planetary and Space Science*, *49*(3–4), 327–336. https://doi.org/10.1016/S0032-0633(00)00154-9

Gurnett, D. A., Kurth, W. S., & Granroth, L. J. (1997). Galileo Orbiter Jupiter: GO-J-PWS-2-REDR-RTS-SA-FULL-V1.0, NASA PDS Planetary Plasma Interaction (PPI) Node. Version 2 [Dataset]. https://doi.org/10.17189/1519682

Gurnett, D. A., Kurth, W. S., Menietti, J. D., & Persoon, A. M. (1998). An unusual rotationally modulated attenuation band in the Jovian hectometric radio emission spectrum. *Geophysical Research Letters*, *25*(11), 1841–1844. https://doi.org/10.1029/98GL01400

Gurnett, D. A., Kurth, W. S., Roux, A., & Bolton, S. J. (1997). Absence of a magnetic-field signature in plasma-wave observations at Callisto. *Nature*, *387*(6630), 261–262. https://doi.org/10.1038/387261a0

Gurnett, D. A., Kurth, W. S., Roux, A., Bolton, S. J., & Kennel, C. F. (1996). Evidence for a magnetosphere at Ganymede from plasma-wave observations by the Galileo spacecraft. *Nature*, *384*(6609), 535–537. https://doi.org/10.1038/384535A0

Gurnett, D. A., Kurth, W. S., Shaw, R. R., Roux, A., Gendrin, R., Kennel, C. F., et al. (1992). The Galileo plasma wave investigation. *Space Science Reviews*, *60*(1–4), 341–355. https://doi.org/10.1007/BF00216861

Gurnett, D. A., Persoon, A. M., Kurth, W. S., Roux, A., & Bolton, S. J. (2000). Plasma densities in the vicinity of Callisto from Galileo plasma wave observations. *Geophysical Research Letters*, *27*(13), 1867–1870. https://doi.org/10.1029/2000GL003751

Hess, S., Cecconi, B., & Zarka, P. (2008). Modeling of Io-Jupiter decameter arcs, emission beaming and energy source. *Geophysical Research Letters*, *35*(13), L13107. https://doi.org/10.1029/2008GL033656

Huebner, W. F., Keady, J. J., & Lyon, S. P. (1992). Solar photo rates for planetary atmospheres and atmospheric pollutants. *Astrophysics and Space Science*, *195*(1), 1–294. https://doi.org/10.1007/BF00644558

Huybrighs, H. L. F., Roussos, E., Blöcker, A., Krupp, N., Futaana, Y., Barabash, S., et al. (2020). An active plume eruption on Europa during Galileo flyby E26 as indicated by energetic proton depletions. *Geophysical Research Letters*, *47*(10), e2020GL087806. https://doi.org/10.1029/2020GL087806

Jia, X., Kivelson, M. G., Khurana, K. K., & Kurth, W. S. (2018). Evidence of a plume on Europa from Galileo magnetic and plasma wave signatures. *Nature Astronomy*, *2*(6), 459–464. https://doi.org/10.1038/s41550-018-0450-z

Jia, X., Walker, R. J., Kivelson, M. G., Khurana, K. K., & Linker, J. A. (2008). Three-dimensional MHD simulations of Ganymede's magnetosphere. *Journal of Geophysical Research*, *113*(A6), A06212. https://doi.org/10.1029/2007JA012748

Jia, X., Walker, R. J., Kivelson, M. G., Khurana, K. K., & Linker, J. A. (2009). Properties of Ganymede's magnetosphere inferred from improved three-dimensional MHD simulations. *Journal of Geophysical Research*, *114*(A9), A09209. https://doi.org/10.1029/2009JA014375

Khurana, K. K., Pappalardo, R. T., Murphy, N., & Denk, T. (2007). The origin of Ganymede's polar caps. *Icarus*, *191*(1), 193–202. https://doi.org/10.1016/j.icarus.2007.04.022

Kimura, T., Tsuchiya, F., Misawa, H., Morioka, A., & Nishimura, Y. (2011). Direct and indirect generation of Jovian quasiperiodic radio bursts by relativistic electron beams in the polar magnetosphere. *Journal of Geophysical Research*, *116*(3), A03202. https://doi.org/10.1029/2010JA016119

Kimura, T., Tsuchiya, F., Misawa, H., Morioka, A., & Nozawa, H. (2008a). Occurrence and source characteristics of the high-latitude components of Jovian broadband kilometric radiation. *Planetary and Space Science*, *56*(8), 1155–1168. https://doi.org/10.1016/J.PSS.2008.03.001

Kimura, T., Tsuchiya, F., Misawa, H., Morioka, A., & Nozawa, H. (2008b). Radiation characteristics of quasi-periodic radio bursts in the Jovian high-latitude region. *Planetary and Space Science*, *56*(15), 1967–1976. https://doi.org/10.1016/J.PSS.2008.09.021

Kivelson, M. G., Bagenal, F., Kurth, W. S., Neubauer, F. M., Paranicas, C., & Saur, J. (2004). Magnetospheric interactions with satellites. In F. Bagenal (Ed.), *Jupiter: The planet, satellites and magnetosphere* (Vol. 21, pp. 513–536). Cambridge University Press.

Kliore, A. J. (1998). Satellite atmospheres and magnetospheres. *Highlights of Astronomy*, *11*(2), 1065–1069. https://doi.org/10.1017/S1539299600019602

Kliore, A. J., Anabtawi, A., Herrera, R. G., Asmar, S. W., Nagy, A. F., Hinson, D. P., & Flasar, F. M. (2002). Ionosphere of Callisto from Galileo radio occultation observations. *Journal of Geophysical Research*, *107*(A11), SIA19-1–SIA19-7. https://doi.org/10.1029/2002JA009365

Kopp, A., & Ip, W.-H. (2002). Resistive MHD simulations of Ganymede's magnetosphere 1. Time variabilities of the magnetic field topology. *Journal of Geophysical Research*, *107*(A12), 1490. https://doi.org/10.1029/2001JA005071

Kurth, W. S., Bolton, S. J., Gurnett, D. A., & Levin, S. (1997). A determination of the source of Jovian hectometric radiation via occultation by Ganymede. *Geophysical Research Letters*, *24*(10), 1171–1174. https://doi.org/10.1029/97GL00988

Kurth, W. S., Gurnett, D. A., Persoon, A. M., Roux, A., Bolton, S. J., & Alexander, C. J. (2001). The plasma wave environment of Europa. *Planetary and Space Science*, *49*(3–4), 345–363. https://doi.org/10.1016/S0032-0633(00)00156-2

Leblanc, F., Oza, A. V., Leclercq, L., Schmidt, C., Cassidy, T., Modolo, R., et al. (2017). On the orbital variability of Ganymede's atmosphere. *Icarus*, *293*, 185–198. https://doi.org/10.1016/J.ICARUS.2017.04.025

Li, J., Gudipati, M. S., & Yung, Y. L. (2020). The influence of Europa's plumes on its atmosphere and ionosphere. *Icarus*, *352*, 113999. https://doi.org/10.1016/J.ICARUS.2020.113999

Liuzzo, L., Poppe, A. R., Paranicas, C., Nénon, Q., Fatemi, S., & Simon, S. (2020). Variability in the energetic electron bombardment of Ganymede. *Journal of Geophysical Research: Space Physics*, *125*(9), e2020JA028347. https://doi.org/10.1029/2020JA028347

Louarn, P., Allegrini, F., McComas, D. J., Valek, P. W., Kurth, W. S., André, N., et al. (2017). Generation of the Jovian hectometric radiation: First lessons from Juno. *Geophysical Research Letters*, *44*(10), 4439–4446. https://doi.org/10.1002/2017GL072923

Louarn, P., Allegrini, F., McComas, D. J., Valek, P. W., Kurth, W. S., André, N., et al. (2018). Observation of electron conics by Juno: Implications for radio generation and acceleration processes. *Geophysical Research Letters*, *45*(18), 9408–9416. https://doi.org/10.1029/2018GL078973

Louis, C. K., Hess, S. L. G., Cecconi, B., Zarka, P., Lamy, L., Aicardi, S., & Loh, A. (2019). ExPRES: An exoplanetary and planetary radio emission simulator. *Astronomy and Astrophysics*, *627*, A30. https://doi.org/10.1051/0004-6361/201935161

Marques, M. S., Zarka, P., Echer, E., Ryabov, V. B., Alves, M. V., Denis, L., & Coffre, A. (2017). Statistical analysis of 26 yr of observations of decametric radio emissions from Jupiter. *Astronomy & Astrophysics*, *604*, A17. https://doi.org/10.1051/0004-6361/201630025

McGrath, M. A., Jia, X., Retherford, K., Feldman, P. D., Strobel, D. F., & Saur, J. (2013). Aurora on Ganymede. *Journal of Geophysical Research: Space Physics*, *118*(5), 2043–2054. https://doi.org/10.1002/JGRA.50122

McGrath, M. A., Lellouch, E., Strobel, D. F., Feldman, P. D., & Johnson, R. E. (2004). Satellite atmospheres. In *Jupiter: The planet, satellites and magnetosphere* (pp. 457–483). Cambridge University.

Menietti, J. D., Gurnett, D. A., Hospodarsky, G. B., Higgins, C. A., Kurth, W. S., & Zarka, P. (2003). Modeling radio emission attenuation lanes observed by the Galileo and Cassini spacecraft. *Planetary and Space Science*, *51*(9–10), 533–540. https://doi.org/10.1016/S0032-0633(03)00078-3

Piker, C., Granroth, L., Mukherjee, J., Pisa, D., Cecconi, B., Kopf, A., & Faden, J. (2019). Lightweight federated data networks with das2 tools. *Earth and Space Science*. Open Archive. https://doi.org/10.1002/essoar.10500359.1

Poppe, A. R., Fatemi, S., & Khurana, K. K. (2018). Thermal and energetic ion dynamics in Ganymede's magnetosphere. *Journal of Geophysical Research: Space Physics*, *123*(6), 4614–4637. https://doi.org/10.1029/2018JA025312

Shematovich, V. I., & Johnson, R. E. (2001). Near-surface oxygen atmosphere at Europa. *Advances in Space Research*, *27*(11), 1881–1888. https://doi.org/10.1016/S0273-1177(01)00299-X

Shematovich, V. I., Johnson, R. E., Cooper, J. F., & Wong, M. C. (2005). Surface-bounded atmosphere of Europa. *Icarus*, *173*(2), 480–498. https://doi.org/10.1016/J.ICARUS.2004.08.013

Vorburger, A., Fatemi, S., Galli, A., Liuzzo, L., Poppe, A. R., & Wurz, P. (2022). 3D Monte-Carlo simulation of Ganymede's water exosphere. *Icarus*, *375*, 114810. https://doi.org/10.1016/J.ICARUS.2021.114810

Vorburger, A., Wurz, P., Lammer, H., Barabash, S., & Mousis, O. (2015). Monte-Carlo simulation of Callisto's exosphere. *Icarus*, *262*, 14–29. https://doi.org/10.1016/J.ICARUS.2015.07.035

Yasuda, R., Kimura, T., Misawa, H., Tsuchiya, T., Cecconi, B., Kasaba, Y., et al. (2024). rikuto-yasuda/icymoon_raytracing: yasudaetal_2024 [Software]. *Zenodo*. https://doi.org/10.5281/zenodo.10969132

Zarka, P. (2004). Radio and plasma waves at the outer planets. *Advances in Space Research*, *33*(11), 2045–2060. https://doi.org/10.1016/J.ASR.2003.07.055